Stable long-term chronic brain mapping at the single-neuron level

Tian-Ming Fu[1,3], Guosong Hong[1,3], Tao Zhou[1,3], Thomas G Schuhmann[2], Robert D Viveros[2] & Charles M Lieber[1,2]

Stable *in vivo* mapping and modulation of the same neurons and brain circuits over extended periods is critical to both neuroscience and medicine. Current electrical implants offer single-neuron spatiotemporal resolution but are limited by such factors as relative shear motion and chronic immune responses during long-term recording. To overcome these limitations, we developed a chronic *in vivo* recording and stimulation platform based on flexible mesh electronics, and we demonstrated stable multiplexed local field potentials and single-unit recordings in mouse brains for at least 8 months without probe repositioning. Properties of acquired signals suggest robust tracking of the same neurons over this period. This recording and stimulation platform allowed us to evoke stable single-neuron responses to chronic electrical stimulation and to carry out longitudinal studies of brain aging in freely behaving mice. Such advantages could open up future studies in mapping and modulating changes associated with learning, aging and neurodegenerative diseases.

Stable mapping and modulation of the same neural network with cellular spatiotemporal resolution over months to years could impact work focused on questions such as how existing neurons evolve into neural circuits with diverse dynamics through learning and developmental processes[1–3]. Moreover, such advances could improve brain–machine interfaces (BMIs) by enabling reliable decoding from individual neurons versus ensemble averages of large population activities for prosthetic applications[4–8]. In addition, stable mapping and modulation could enable longitudinal, rather than cross-sectional, studies of aging-associated brain changes and cognitive decline caused by neurodegenerative diseases[9–12].

Approaches such as noninvasive brain imaging[13,14] and surface[15] and endovascular probes[16] can provide long-term monitoring of brain activity, although their low spatiotemporal resolutions preclude investigations of circuit dynamics at the cellular level. Optical imaging techniques can achieve neuron-resolution mapping but are limited in terms of penetration depth, image acquisition rates and genetic incorporation of labels[17]. On the other hand, electrical implants such as silicon probes and microwire tetrodes[18–21] can provide spatiotemporal mapping at the single-neuron level from deep brain regions. However, mechanical mismatch and chronic immune responses—which result in shear motion, glial scar formation and neuron depletion at probe–brain interfaces—lead to degradation of recording and stimulation capabilities typically over days to weeks[6–8,22–24]. Some researchers claim to have achieved months or years of stable recordings from a small fraction of electrical implants[25–27], but others report instability within a day or a week using the same types of probes[8,23]. Practically, probes are repositioned to compensate for recording instability[20,21,23,24,28], although this causes further tissue damage and precludes monitoring of the originally targeted neurons. These issues have thus limited the use of implanted probes in long-term studies.

Factors reported to contribute to chronic instability of implanted probes include size and mechanical mismatch with neurons and neural tissue[6,29–31]. Studies focused on reducing probe size[30] have reduced deleterious immune responses, but these smaller probes still exhibit substantial mechanical mismatch with neural tissue. To address these structural and mechanical issues, we have recently described mesh electronics[32–34] with micrometer feature sizes comparable to neuron somata and effective bending stiffness values comparable to those of dense neural tissue. In this work, we demonstrate a chronic recording and stimulation mesh electronics platform that overcomes the limitations of conventional probes and thereby enables consistent and reproducible recording from and stimulation of the same individual neurons *in vivo* for at least 8 months.

RESULTS

Brain injection and recording interface for mesh electronics

We fabricated mesh electronics using standard photolithography procedures[32,33] (**Supplementary Fig. 1**). The overall design (**Supplementary Fig. 2**) consisted of an array of 16 recording or stimulation electrodes at one end addressed individually by metal interconnects and terminated with input–output (I–O) pads at the opposite end of the mesh structure. The interconnects are sandwiched by insulating and biocompatible polymer layers, leaving only the recording and stimulation electrodes in direct contact with brain tissue. The thickness (~800 nm) and width (20 μm) of

[1]Department of Chemistry and Chemical Biology, Harvard University, Cambridge, Massachusetts, USA. [2]John A. Paulson School of Engineering and Applied Sciences, Harvard University, Cambridge, Massachusetts, USA. [3]These authors contributed equally to this work. Correspondence should be addressed to C.M.L. (cml@cmliris.harvard.edu).

RECEIVED 17 MARCH; ACCEPTED 26 JULY; PUBLISHED ONLINE 29 AUGUST 2016; DOI:10.1038/NMETH.3969

the mesh elements yield a low bending stiffness value of ~0.1 nN m, which is comparable to the stiffness value of neural tissue[35] and correlates with a low immune response[32,34].

An overview of our approach (**Fig. 1**) highlights the flexible open mesh electronics and lightweight instrument interface. First, we stereotactically injected the mesh electronics through a capillary needle into a targeted brain region, achieving a positioning precision of ~20 μm (ref. 33) (**Supplementary Figs. 3** and **4a**,**b**), an extended morphology and integration of the mesh structure with neurons (**Fig. 1a**). Microcomputed tomography (micro-CT) postinjection (**Fig. 1b**) confirmed an extended morphology along the injection direction. Second, we unfolded and electrically connected the I–O pads of mesh electronics to a lightweight (~0.2 g) flexible flat cable (FFC) using printed conductive ink[33] (**Fig. 1c** and **Supplementary Fig. 4c**,**d**). The flexibility of the electronics was apparent (yellow arrow, **Fig. 1c**) as the rolled-up mesh 'sags' between the exit point on the brain and skull and the FFC. We fixed the FFC, which is plugged into recording instrumentation, to the mouse skull and folded it to minimize its size (**Fig. 1b**,**d** and **Supplementary Fig. 4e**,**f**). Finally, we did not adjust the positions of mesh electronics over the course of our chronic experiments following implantation.

Long-term brain activity mapping at the single-neuron level

We assessed initial long-term recording stability from 16-channel mesh electronics spanning the hippocampus (HIP) and somatosensory cortex (CTX) of a mouse. Representative multiplexed recordings from the same awake mouse at 2 and 4 months postinjection yielded well-defined local field potentials (LFPs) in all 16 channels with modulation amplitudes of ~300 μV and single-unit spikes from 14 channels (**Fig. 2a**). Focusing on single-unit spikes, we found that different channels exhibited stable amplitudes and signal-to-noise ratios (SNRs) across this 2-month period (**Fig. 2a**). Cross-channel correlation maps of LFPs and single-unit spikes (**Supplementary Fig. 5**) showed similar patterns over this time period. The constant single-unit amplitudes and similar spike firing patterns over time suggested that these data might correspond to signals from the same neurons and neural circuits. We further address this central issue below with studies extending to 8 months.

Multiplexed data recorded over at least 6-month periods from four mice (**Fig. 2b** and **Supplementary Fig. 6e**; mice 1–4) showed an initial amplitude increase followed by stable spike amplitudes ~6 weeks postinjection. Representative chronic single-unit recording traces from one electrode (Mouse 4–Channel A) highlighted several points. First, peak-to-peak spike amplitudes increased from ~30 μV (1 week) to ~130 μV (2 months) and thereafter remained stable to at least 6 months postinjection, with overall firing rate approximately constant across the entire period (**Supplementary Fig. 6a**). Second, we observed two distinct clusters of sorted spikes with visually stable waveforms indicative of two neurons (**Supplementary Fig. 6b**). Waveform autocorrelation analyses[23] showed a large percentage of similarity both within the same recording session and across 6 months (**Supplementary Fig. 6c**,**d**). Together, these results suggest stable single-neuron recording during this extended time period. The electrode interfacial impedances (**Fig. 2c** and **Supplementary Fig. 6f**) exhibited relatively constant values (mean ~300 kΩ) over time, in contrast with other brain implants with reported electrode impedance fluctuations attributed to chronic immune response[6,22].

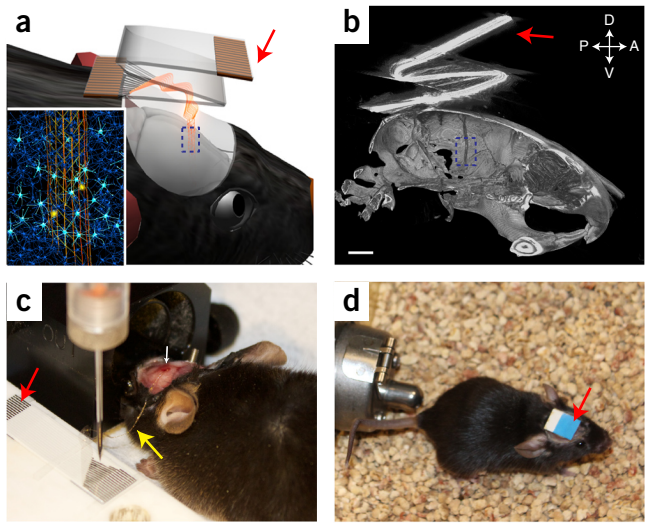

Figure 1 | Syringe-injectable mesh electronics for chronic brain mapping and modulation. (**a**) Schematic showing a mouse with stereotaxically injected mesh electronics (gold) bonded through conductive ink (black lines) printing to a flexible flat cable (FFC, red arrow), which is folded afterwards to minimize its profile. Inset, a zoomed-in view of the blue dashed box illustrating seamless integration of the mesh electronics with neural network. The gold lines and the white and yellow circles represent metal interconnects and recording and stimulation electrodes, respectively. (**b**) Microcomputed tomography (micro-CT) image showing a lateral view of a mouse head with injected mesh electronics (blue dashed box) and folded FFC (red arrow). Axes labeled with A, P, D and V represent anterior, posterior, dorsal and ventral anatomical directions, respectively. Scale bar, 2 mm. (**c**) Picture showing the conductive ink (black lines) printing process to electrically connect the mesh electronics (yellow arrow) to the FFC (red arrow) during surgery. The white arrow highlights the implantation site. (**d**) Picture showing a freely behaving mouse with mesh electronics injected and FFC attached (red arrow). The width of the FFC in **c** and **d** is ~8 mm.

To assess the long-term single-neuron signal stability and provide insight into the short-term amplitude increase, we carried out time-dependent histology studies. In horizontal brain slices at 6 and 12 weeks postinjection (**Fig. 2d**), axonal projections and somata were present within the mesh electronics. Signals of axonal projections and somata were close to and at background levels near the outer and inner surfaces of the mesh electronics, respectively (**Fig. 2e**). Astrocytes and microglia exhibited a similar distribution (**Fig. 2e** and **Supplementary Fig. 7**).

The 2-week-postinjection data provided insight into the initial increase in spike amplitude. Specifically, cell density within the mesh electronics was low from acute needle insertion damage, although we could detect some axonal projections, astrocytes and microglia in this region (**Fig. 2d**,**e** and **Supplementary Fig. 7**). Astrocytes and microglia were slightly enriched up to 100–300 μm from the probe surface. Hence, the observed amplitude increase during the first weeks postinjection could be associated with recovery from acute implantation damage via gradual removal of astrocytes and microglia.

Chronic tracking of individual neurons

We carried out statistical analyses to confirm the chronic stability of recorded neuron and neural circuit signals. Principal component analysis (PCA), which can define the number and stability of recorded single-neuron signals over time[28,30], of representative sorted spikes (**Fig. 3a**) showed the same three clusters with

nearly constant positions in the first and second principal component plane (PC1–PC2) from 5 through 34 weeks postinjection. Time-dependent averaged spike waveforms (**Fig. 3b**), waveform auto- and cross-correlation[23] (**Supplementary Fig. 8a**) and L ratio analyses[36] (**Supplementary Table 1**) further demonstrated good unit separation and high stability over this time period.

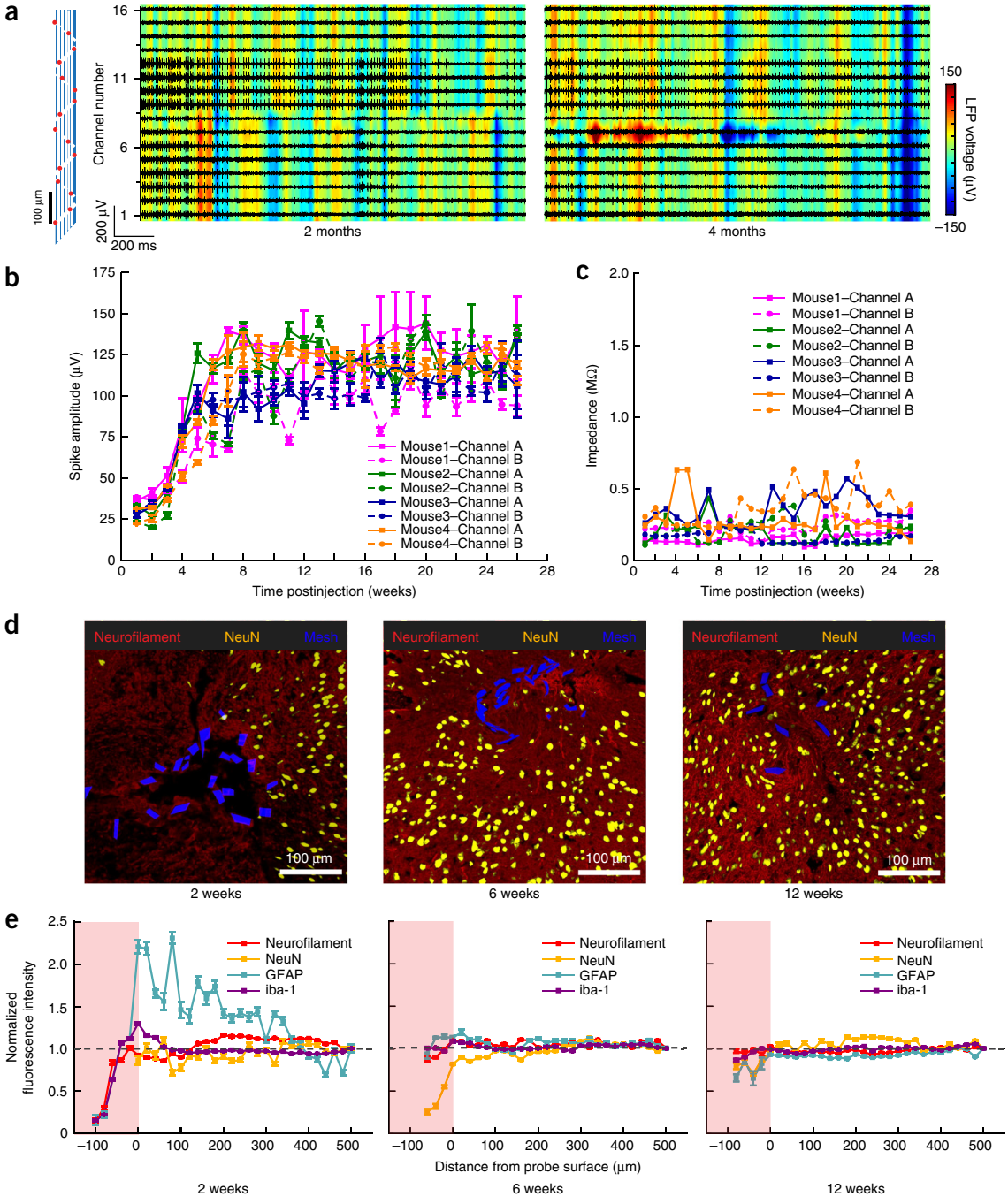

Figure 2 | Long-term stable recording without signal degradation over six months and immunohistochemistry staining of mesh electronics–brain tissue interface. (**a**) Representative 16-channel local field potential (LFP; heat maps) with amplitudes color-coded according to the color bar on the far right and single-unit spike (traces) mapping from the same mouse at 2 (left) and 4 (right) months postinjection. The *x*-axes show the recording time while the *y*-axes represent the channel number of each recording electrode with relative position marked by red dots in the schematic (leftmost panel). (**b**) Time evolution of average spike amplitudes of representative channels from four different mice. Mouse 1 represents the recordings shown in **a**, with Channels A and B denoting channels 10 and 3, respectively. Mouse 2–Channel A, Mouse 2–Channel B and Mouse 3–Channel A were used for analyses shown in **Figures 3** and **5** and in **Supplementary Figures 10** and **12**. Mouse 4–Channel A represents the recordings shown in **Supplementary Figure 6**. (**c**) Time-dependent impedance values at 1 kHz of the channels shown in **b**. (**d**) Immunohistochemical staining images of horizontal brain slices at 2 (left, hippocampus (HIP)), 6 (middle, cortex (CTX)) and 12 weeks (right, CTX) postinjection. Red, yellow and blue colors correspond to neurofilaments, NeuN and mesh electronics, respectively. Scale bars, 100 µm. (**e**) Neurofilament (red), NeuN (yellow), GFAP (cyan) and iba-1 (purple) fluorescence intensity normalized against background values (gray dashed horizontal lines) plotted versus distance from the interface. The pink-shaded regions indicate the interior of the mesh electronics. All error bars in this figure reflect ±1 s.e.m.

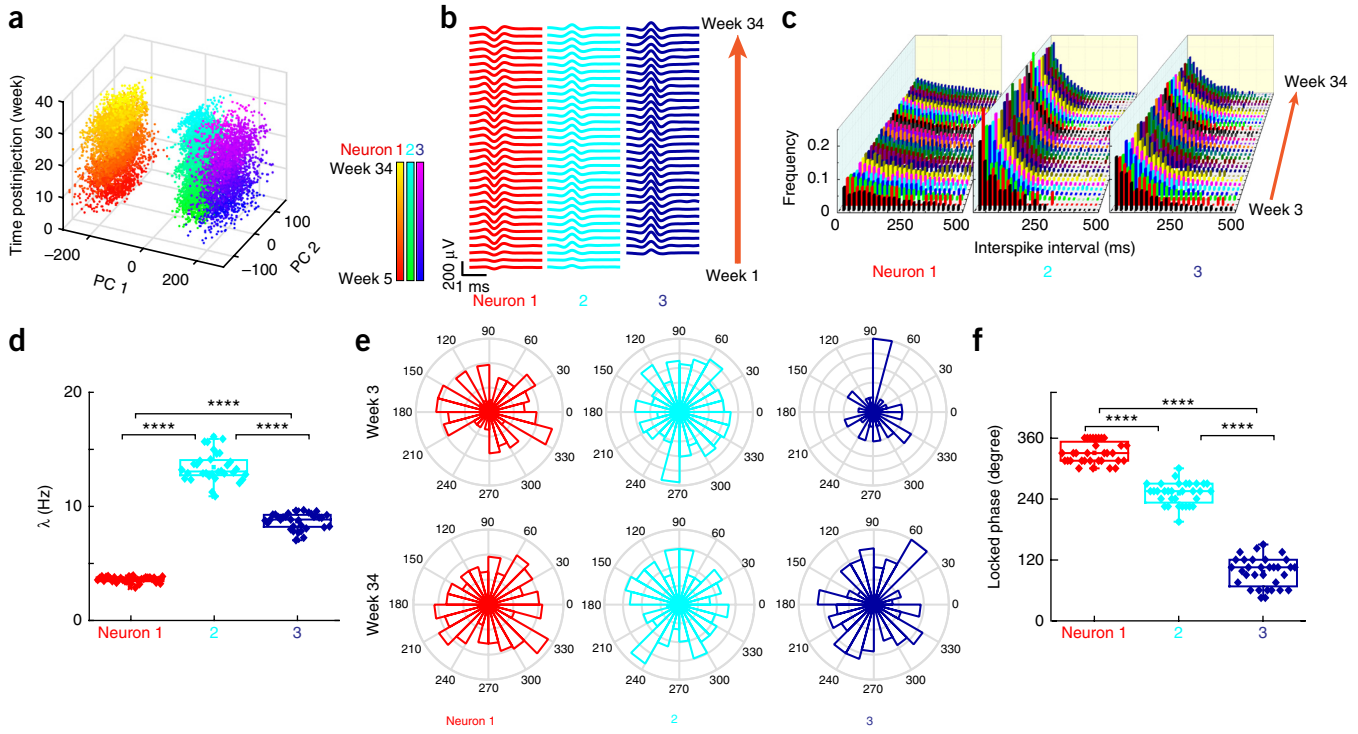

Figure 3 | Consistent tracking of the same group of neurons. (**a**) Time evolution of representative single-unit spikes of Mouse 2–Channel A shown in **Figure 2** clustered by principal component analysis (PCA) over 8 months postinjection. The *x*- and *y*-axes denote the first and second principal components, respectively, and the *z*-axis indicates postinjection time. The color scale bars show the corresponding postinjection time points from 5 to 34 weeks (8 months) of the 3D PCA plots. (**b**) Timecourse analysis of average spike waveforms from each PCA cluster shown in **a**. (**c**) Time evolution of interspike interval (ISI) histograms of each of the three neurons identified in **a** from 3 to 34 weeks. Bin size, 20 ms. (**d**) Scatter plot with analysis of variance (ANOVA) of the firing parameter (n = 32 for each neuron), λ, obtained by fitting each ISI distribution profile shown in **c** to an exponential decay. (**e**) Polar plots showing the phase locking of single-unit spikes to theta oscillations (4–8 Hz) of LFPs in HIP for each of the three neurons in **a** at 3 and 34 weeks. (**f**) Scatter plot with ANOVA test of the locked phase angle (n = 32 for each neuron). For **d** and **f**, the open rectangles and bars indicate 25/75 and 0/100 percentiles, respectively. **** indicates P value < 0.0001.

We characterized the individual neuron firing dynamics by the interspike interval (ISI) distributions for the three identified neurons (**Fig. 3c**; see Online Methods). These ISI histograms exhibited stable and distinct distributions with characteristic 2- to 3-ms refractory periods[37] (**Supplementary Fig. 9**) over 8 months. Analysis of the variance (ANOVA) on the firing parameter, λ (reflecting neuron firing rates[37]), obtained from exponential fits to each ISI histogram showed a significant difference (P value < 0.0001) between any two neurons (**Fig. 3d**), thus confirming that the same neurons were followed over this 8-month period. We carried out similar analyses for another channel from the same mesh (**Supplementary Figs. 8** and **10**, Mouse 2–Channel B) and one channel from another mouse (**Supplementary Figs. 8** and **10**, Mouse 3–Channel A). Results showed unchanged principal components (**Supplementary Fig. 10a**,**b**), L ratios demonstrating good unit separation (**Supplementary Table 1**), constant spike waveforms supported by auto- and cross-correlation (**Supplementary Figs. 8b**,**c** and **10c**,**d**), and stable ISI histograms and firing parameters (**Supplementary Fig. 10e**–**h**).

To test the potential for stable recording from neural circuits, we analyzed phase locking between single-neuron firings and LFPs with a focus on HIP data, which have been reported to show phase locking[38]. We found clear evidence for stable phase locking at distinct angles from 3 to 34 weeks postinjection for each of the three neurons identified with means of 330°, 250° and 95° (**Fig. 3e**,**f**; **Supplementary Fig. 11** and **Supplementary Table 2**)[39]. Thus, mesh electronics can record from the same neural circuit over 8 months[40].

Multisite recording from different brain regions

Multiple meshes can be combined to stably record from distinct brain regions. We connected the I–O pads from two meshes to the same FFC (**Fig. 4a**,**b**) without significant increase in the interface weight. Multiplexed LFP recordings from mesh electronics implanted in the motor CTX (red) and HIP (blue) of opposite cerebral hemispheres showed similar modulation within a probe but distinct signals between probes (**Fig. 4c**). Both probes exhibited stable LFP amplitudes across at least 2 months (**Fig. 4c**). Representative single-unit spike traces (**Fig. 4d**) demonstrated consistent chronic firing dynamics, and spike sorting (**Fig. 4d**) showed stable amplitudes and consistent cluster waveforms (two identified neurons in CTX and four in HIP) over this time period.

Multifunctional mesh for chronic stimulation and recording

We expanded the capabilities of mesh electronics by incorporating 150-µm-diameter low-impedance stimulation electrodes (**Fig. 4e**), and we chronically stimulated and recorded from 4 to 14 weeks postinjection. First, a peristimulus spike raster plot (**Fig. 4f**) showed an increased firing rate following stimulation. Second, histograms of first-spike latency following stimulation

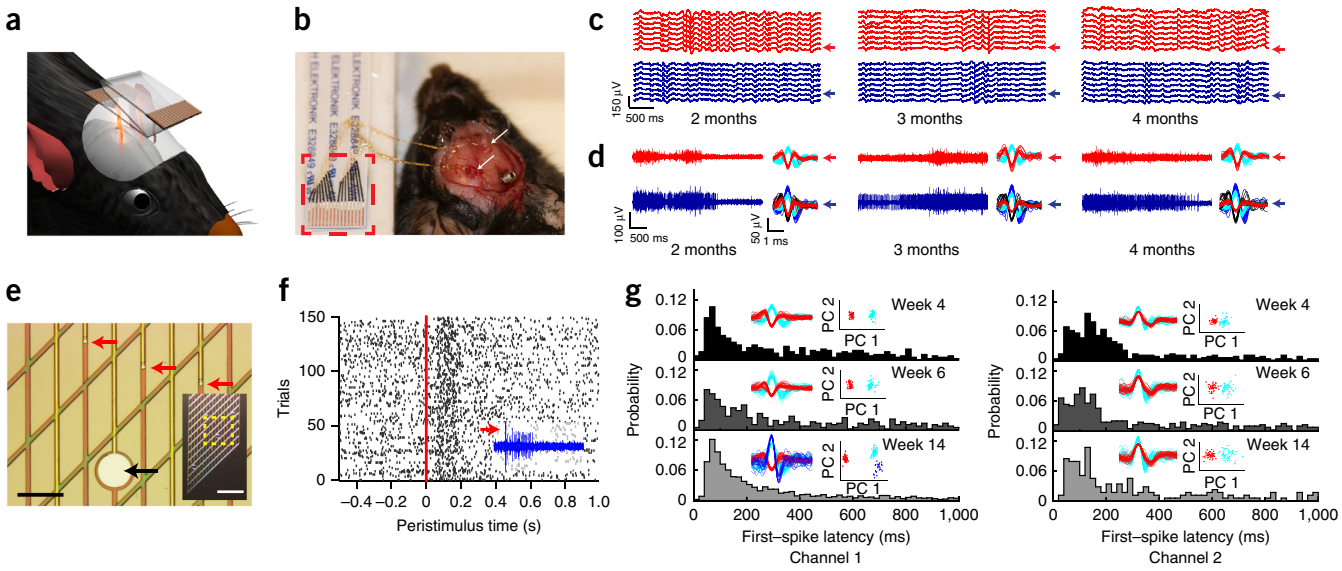

Figure 4 | Multisite and multifunctional mesh electronics. (**a**) Schematic and (**b**) photo showing two mesh electronics (white arrows) injected into different brain regions (motor CTX of the right cerebral hemisphere and HIP of the left hemisphere) of the same mouse. The two mesh probes were bonded to the same FFC (red dashed box in **b**). The width of the FFC in **b** is ~8 mm. (**c**) Multiplexed LFP and (**d**) single-unit recordings along with sorted spikes from the motor CTX (red traces) of one hemisphere and the HIP (blue traces) from the contralateral hemisphere. The three columns correspond to data recorded at 2 (left), 3 (middle) and 4 (right) months postinjection. The red and blue arrows in **c** highlight the channels corresponding to the representative spike trains shown in **d**. (**e**) Photograph showing typical mesh electronics before releasing from substrate with unipolar stimulation electrodes (black arrow) and recording electrodes (red arrows). Scale bar, 200 μm. Inset, zoomed-out photograph with yellow dashed box representing the area of **e**. Inset scale bar, 1 mm. (**f**) Peristimulus raster plot showing spike events (black ticks) of 150 stimulation trials (red solid line, stimulation pulse). Inset, representative recorded spike trains from –0.125 to 0.875 s. The red arrow indicates the stimulation pulse. (**g**) First-spike latency distributions of stimulus-evoked firings recorded from two different electrodes (channels 1 and 2) located in the same cerebral hemisphere but with progressively increasing distance from the stimulation electrode at 4, 6 and 14 weeks postinjection. Spike sorting and PCA clustering results are displayed as insets. The color of each sorted spike cluster corresponds to that of each PCA group.

for two recording electrodes (**Fig. 4g**, channels 1 and 2) exhibited consistent distributions from 4 to 14 weeks in weekly stimulation trials. Control data recorded from a second mesh implanted in the contralateral hemisphere showed no stimulation-evoked response. Third, spike-sorting and PCA analyses of channels 1 and 2 (**Fig. 4g**, insets) confirmed stable recording of two unique neurons for both electrodes, although a third neuron was identified at about 14 weeks in channel 1.

Longitudinal studies of aging at the single-neuron level

The long-term recording stability with mesh electronics can enable longitudinal studies of aging-associated changes at single-neuron and neural-circuit levels. On account of chronic instability, previous research has been limited to longitudinal studies with low spatiotemporal resolution[9,14] or high-resolution electrophysiology studies comparing different subjects[9,10]. We tracked the time evolution of firing dynamics and spike characteristics of individual neurons before and after two mice entered middle age at 10–12 months[41]. These data revealed aging-associated neuronal changes (**Fig. 5** and **Supplementary Fig. 12**). First, analyses of ISI histograms showed firing rate declines for mice aged ~48 weeks and older with individual neurons exhibiting distinct time-dependent changes (**Fig. 5a**,**b** I and **Supplementary Fig. 12e**,**f**). For example, neurons 2 and 3 of Mouse 2–Channel A (**Fig. 5a**, I) showed decreases in firing rate starting at ~48 weeks, while the firing of neuron 1 was relatively unaffected. Similar decreases were seen for Mouse 3–Channel A (**Fig. 5b**, I). Second, we found no systematic changes in electrode impedances (**Supplementary Fig. 12g**), and histology study showed uniform distributions of neuronal somata, axonal projections, astrocytes and microglia through the mesh electronics interior at ~1 year postinjection (**Supplementary Fig. 12h**,**i**). These results suggest minimal or no degradation of recording electrodes and correspondingly argue that the observed firing rate decreases are intrinsic to individual neurons. Third, quantitative analyses of sorted spike waveforms (**Fig. 5a**,**b**, II) revealed a neuron-specific increase of peak-to-trough time starting at ~48 weeks of mouse age; that is, neurons 2 and 3 of Mouse 2–Channel A (**Fig. 5a**, II) both showed increases in peak-to-trough time with little or no increase observed for neuron 1. These increases in single-neuron peak-to-trough times coincided temporally with the firing rate decreases and were especially prominent for neurons with larger firing rate decreases (**Fig. 5a**,**b**).

Chronic recording from freely behaving mice

For chronic studies of freely behaving mice, we directly bonded mesh electronics to a preamplifier (preamp) connector following injection (see Online Methods). The lightweight interface was only 1.0 g with the preamp plugged in (0.35 g without preamp), allowing data acquisition through a flexible cable that did not restrict animal motion (**Fig. 6a** and **Supplementary Video 1**). The interface had minimal impact on the housed animal without preamp given its low profile and weight. We grouped single-unit recordings from five channels at 5 weeks postinjection (**Fig. 6b**) into periods when the mouse was whisking food (I) or foraging (II) in a novel environment. The two channels located in CTX barrel

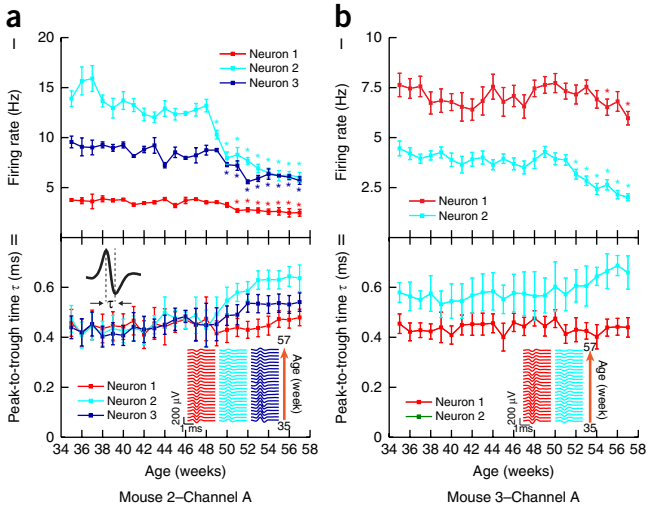

Figure 5 | Longitudinal study of brain aging at the single-neuron level. (**a**,**b**) Time evolution of average spike firing rate (I) and average peak-to-trough time τ (defined in upper left inset in **a**, II) with average spike waveforms shown as bottom-right insets (II) of each neuron identified from the PCA clusters in **Supplementary Figure 12** from representative channels of Mouse 2 (**a**) and 3 (**b**), respectively. The *x*-axes show the corresponding mouse ages in all panels. The error bars in I show fitting errors, and * indicates statistically significant ($P < 0.05$, double-sided *t*-test, $n = 50$) decrease of firing rate compared with that at age of 48 weeks. The error bars in II show ± 1 s.d.

field (channels D and E) consistently showed behavior-related firing rate increases during whisking, while the other three channels exhibited no significant changes across the 27-week measurement course (**Fig. 6c** and **Supplementary Fig. 13**). Analyses of sorted spikes within the same recording session (**Supplementary Fig. 13a**) revealed comparable fluctuations in the intrinsic recording noise (**Supplementary Fig. 13b** and **Supplementary Table 3**) and stable unit isolation (**Supplementary Fig. 13c**). Phase-locking analyses between single-unit firings in barrel CTX (channel D) and theta-band LFP oscillations in HIP (channel A) at different time points indicated relatively constant locking at ~300° during active whisking versus no identifiable phase coherence during foraging (**Fig. 6d**). These findings are consistent with a pathway linking the barrel field that receives vibrissa input and HIP with higher-order processing of texture information, in agreement with recent reports[42,43].

DISCUSSION

In summary, our chronic *in vivo* mesh electronics recording and stimulation platform has achieved stable multiplexed LFP and single-unit spike recordings from mouse HIP and CTX with tracking of the same neurons and neural circuits up to 8 months. These results contrast with those of conventional brain probes that generally exhibit spike shape changes over days to weeks[6–8,22–24], although occasionally long-term stability can be obtained from one or a small numbers of electrodes[25–27]. To the best of our knowledge, consistent and reproducible stable chronic recording and stimulation from the same single neurons or neural circuits has previously been unattainable for longer than several weeks.

Mechanistically, these findings correlate with the comparable bending stiffness values for the mesh electronics and neural tissue, which minimize or eliminate relative shear motion of the electronics inside the brain since the implant is effectively decoupled from the I–O fixed to skull. In addition, near-natural distributions of neurons, axons and glial cells at the mesh electronics surface contrast with a 50- to 200-µm region of neuron depletion around conventional brain implants[22]; these near-natural cell distributions substantiated the observed stable single-unit spike amplitudes for the same time periods.

We also observed an amplitude increase at early times postinjection, which is associated with recovery from acute implantation damage. While the units identified at 1 week postinjection remained consistent through the point of reaching a stable amplitude, the somewhat lower percentage of cross-week autocorrelation for some neurons might suggest a contribution from

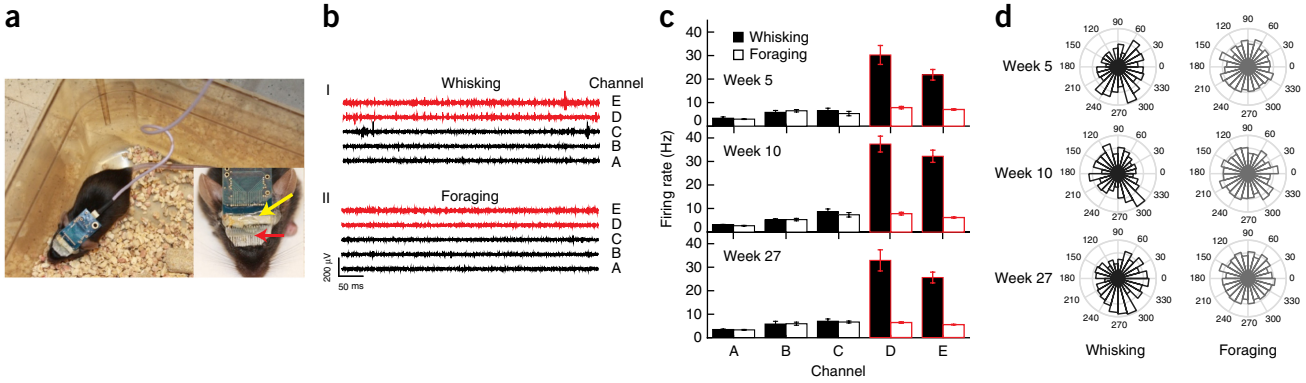

Figure 6 | Chronic recordings from a freely behaving mouse. (**a**) Photograph of a typical freely behaving mouse recording. Voltage amplifier was directly positioned near the mouse head to minimize mechanical noise coupling. A flexible serial peripheral interface (SPI) cable was used to transmit amplified signals to the data acquisition systems. Inset, a zoomed-in view showing the conductive ink (black lines), FFC (red arrow), Omnetics connector (yellow arrow) and the voltage amplifier (blue-green rectangle). The width of the voltage-amplifier is ~1.5 cm. (**b**) Single-unit spike recordings at 5 weeks postinjection from five representative channels, two of which (Channels D and E, shown in red) are located in the somatosensory CTX, when the mouse was whisking food pellets (I) and foraging in the cage (II). (**c**) Bar charts summarizing the changes in firing rate for the same five channels shown in **b** during whisking (black bars) and foraging (white bars) at 5 (top), 10 (middle) and 27 weeks (bottom) postinjection. The two channels (Channels D and E) with whisking-associated neuronal responses are highlighted with red borders. Error bars indicate ± 1 s.e.m. (**d**) Polar plots showing phase locking of single-unit spikes recorded in the CTX barrel field (Channel D) to the theta oscillations (4–8 Hz) of LFPs in the HIP (Channel A) when the mouse was whisking (left column) and foraging (right column) at 5, 10 and 27 weeks.

axon and dendrite regeneration (**Supplementary Fig. 14**). In addition, new clusters appearing in some of the recordings indicate a role for tissue remodeling.

In addition, during brain aging the gradual decrease in firing rate, which correlates inversely with a progressive increase in peak-to-trough time in individual neurons, is not only consistent with impaired long-term potentiation (LTP), decreased $[Ca^{2+}]_i$ baseline and increased after-hyperpolarization (AHP) suggested by cross-sectional rodent studies[11,44,45], but it also reveals details on the evolution of individual neurons that were previously inaccessible.

Lastly, it could be beneficial to increase the number of recording channels and to achieve full-amplitude spikes closer to initial implantation for our mesh platform. A combination of increasing the number and density of electrodes in each mesh probe and multisite injection of several meshes into the same animal provides a feasible strategy for achieving higher multiplexing. On the other hand, initial tests of implantation with reduced needle diameters and injected solution volumes indicate that full-amplitude spikes can be observed in only ~3 weeks. Approaches involving coinjection of stem cells or neurotrophic factors will also be interesting to pursue. Furthermore, biochemical studies directed at better understanding the mechanisms accounting for chronic interpenetration of neuronal cells and projections and observed electrophysiological changes during brain aging will be valuable topics for future investigations. However, the unique capability to record from and stimulate the same neurons and neural circuits over at least 8-month periods already opens up important neurobiology opportunities, including understanding fundamental neural circuit plasticity, reorganization and development during learning, memory formation and aging-associated cognitive decline; and it enables closed-loop BMIs in freely behaving animals via stable single-neuron based decoding and communication.

METHODS

Methods and any associated references are available in the online version of the paper.

Note: Any Supplementary Information and Source Data files are available in the online version of the paper.

ACKNOWLEDGMENTS

We thank J. Huang for help with recording instrumentation, J. Liu and J. Tian for training in chronic surgery, S. Patel for help with data analysis and stimulation implementation, G. Guitchounts and S. Wolff for help in freely behaving mouse recording implementation and data interpretation, and C. Perez Estrada for helpful discussions. C.M.L. acknowledges support from the Air Force Office of Scientific Research, the Star Family and Fidelity Biosciences Funds, and the Harvard University Physical Sciences and Engineering Accelerator award. This work was performed in part at the Harvard University Center for Nanoscale Systems (CNS), a member of the National Nanotechnology Coordinated Infrastructure Network (NNCI), which is supported by the National Science Foundation.

AUTHOR CONTRIBUTIONS

T.-M.F., G.H. and C.M.L. designed the experiments. T.-M.F., G.H., T.Z., T.G.S. and R.D.V. performed the experiments. T.-M.F., G.H., T.Z. and C.M.L. analyzed the data and wrote the paper. All authors discussed the results and commented on the manuscript.

COMPETING FINANCIAL INTERESTS

The authors declare no competing financial interests.

1. Yuste, R. From the neuron doctrine to neural networks. *Nat. Rev. Neurosci.* **16**, 487–497 (2015).
2. Stanley, G.B. Reading and writing the neural code. *Nat. Neurosci.* **16**, 259–263 (2013).
3. Cash, S.S. & Hochberg, L.R. The emergence of single neurons in clinical neurology. *Neuron* **86**, 79–91 (2015).
4. Hochberg, L.R. *et al.* Reach and grasp by people with tetraplegia using a neurally controlled robotic arm. *Nature* **485**, 372–375 (2012).
5. Shenoy, K.V. & Carmena, J.M. Combining decoder design and neural adaptation in brain-machine interfaces. *Neuron* **84**, 665–680 (2014).
6. Bensmaia, S.J. & Miller, L.E. Restoring sensorimotor function through intracortical interfaces: progress and looming challenges. *Nat. Rev. Neurosci.* **15**, 313–325 (2014).
7. Aflalo, T. *et al.* Neurophysiology. Decoding motor imagery from the posterior parietal cortex of a tetraplegic human. *Science* **348**, 906–910 (2015).
8. Perge, J.A. *et al.* Intra-day signal instabilities affect decoding performance in an intracortical neural interface system. *J. Neural Eng.* **10**, 036004 (2013).
9. Grady, C. The cognitive neuroscience of ageing. *Nat. Rev. Neurosci.* **13**, 491–505 (2012).
10. Wang, M. *et al.* Neuronal basis of age-related working memory decline. *Nature* **476**, 210–213 (2011).
11. Yeoman, M., Scutt, G. & Faragher, R. Insights into CNS ageing from animal models of senescence. *Nat. Rev. Neurosci.* **13**, 435–445 (2012).
12. Stam, C.J. Modern network science of neurological disorders. *Nat. Rev. Neurosci.* **15**, 683–695 (2014).
13. Kornblum, H.I. *et al. In vivo* imaging of neuronal activation and plasticity in the rat brain by high resolution positron emission tomography (microPET). *Nat. Biotechnol.* **18**, 655–660 (2000).
14. Poldrack, R.A. & Farah, M.J. Progress and challenges in probing the human brain. *Nature* **526**, 371–379 (2015).
15. Chang, E.F. Towards large-scale, human-based, mesoscopic neurotechnologies. *Neuron* **86**, 68–78 (2015).
16. Oxley, T.J. *et al.* Minimally invasive endovascular stent-electrode array for high-fidelity, chronic recordings of cortical neural activity. *Nat. Biotechnol.* **34**, 320–327 (2016).
17. Hamel, E.J., Grewe, B.F., Parker, J.G. & Schnitzer, M.J. Cellular level brain imaging in behaving mammals: an engineering approach. *Neuron* **86**, 140–159 (2015).
18. Berényi, A. *et al.* Large-scale, high-density (up to 512 channels) recording of local circuits in behaving animals. *J. Neurophysiol.* **111**, 1132–1149 (2014).
19. Scholvin, J. *et al.* Close-packed silicon microelectrodes for scalable spatially oversampled neural recording. *IEEE Trans. Biomed. Eng.* **63**, 120–130 (2016).
20. Yamamoto, J. & Wilson, M.A. Large-scale chronically implantable precision motorized microdrive array for freely behaving animals. *J. Neurophysiol.* **100**, 2430–2440 (2008).
21. Schwarz, D.A. *et al.* Chronic, wireless recordings of large-scale brain activity in freely moving rhesus monkeys. *Nat. Methods* **11**, 670–676 (2014).
22. Polikov, V.S., Tresco, P.A. & Reichert, W.M. Response of brain tissue to chronically implanted neural electrodes. *J. Neurosci. Methods* **148**, 1–18 (2005).
23. Jackson, A. & Fetz, E.E. Compact movable microwire array for long-term chronic unit recording in cerebral cortex of primates. *J. Neurophysiol.* **98**, 3109–3118 (2007).
24. Voigts, J., Siegle, J.H., Pritchett, D.L. & Moore, C.I. The flexDrive: an ultra-light implant for optical control and highly parallel chronic recording of neuronal ensembles in freely moving mice. *Front. Syst. Neurosci.* **7**, 8 (2013).
25. Thompson, L.T. & Best, P.J. Long-term stability of the place-field activity of single units recorded from the dorsal hippocampus of freely behaving rats. *Brain Res.* **509**, 299–308 (1990).
26. Krüger, J., Caruana, F., Volta, R.D. & Rizzolatti, G. Seven years of recording from monkey cortex with a chronically implanted multiple microelectrode. *Front. Neuroeng.* **3**, 6 (2010).
27. Vaidya, M. *et al.* Ultra-long term stability of single units using chronically implanted multielectrode arrays. *Conf. Proc. IEEE Eng. Med. Biol. Soc.* **2014**, 4872–4875 (2014).

28. Dickey, A.S., Suminski, A., Amit, Y. & Hatsopoulos, N.G. Single-unit stability using chronically implanted multielectrode arrays. *J. Neurophysiol.* **102**, 1331–1339 (2009).
29. Karumbaiah, L. *et al.* Relationship between intracortical electrode design and chronic recording function. *Biomaterials* **34**, 8061–8074 (2013).
30. Kozai, T.D.Y. *et al.* Ultrasmall implantable composite microelectrodes with bioactive surfaces for chronic neural interfaces. *Nat. Mater.* **11**, 1065–1073 (2012).
31. Kim, J. *et al.* Next-generation flexible neural and cardiac electrode arrays. *Biomed. Eng. Lett.* **4**, 95–108 (2014).
32. Liu, J. *et al.* Syringe-injectable electronics. *Nat. Nanotechnol.* **10**, 629–636 (2015).
33. Hong, G. *et al.* Syringe injectable electronics: precise targeted delivery with quantitative input/output connectivity. *Nano. Lett.* **15**, 6979–6984 (2015).
34. Xie, C. *et al.* Three-dimensional macroporous nanoelectronic networks as minimally invasive brain probes. *Nat. Mater.* **14**, 1286–1292 (2015).
35. Tyler, W.J. The mechanobiology of brain function. *Nat. Rev. Neurosci.* **13**, 867–878 (2012).
36. Schmitzer-Torbert, N. & Redish, A.D. Neuronal activity in the rodent dorsal striatum in sequential navigation: separation of spatial and reward responses on the multiple T task. *J. Neurophysiol.* **91**, 2259–2272 (2004).
37. Shadlen, M.N. & Newsome, W.T. The variable discharge of cortical neurons: implications for connectivity, computation, and information coding. *J. Neurosci.* **18**, 3870–3896 (1998).
38. Skaggs, W.E., McNaughton, B.L., Wilson, M.A. & Barnes, C.A. Theta phase precession in hippocampal neuronal populations and the compression of temporal sequences. *Hippocampus* **6**, 149–172 (1996).
39. Siapas, A.G., Lubenov, E.V. & Wilson, M.A. Prefrontal phase locking to hippocampal theta oscillations. *Neuron* **46**, 141–151 (2005).
40. Khodagholy, D. *et al.* NeuroGrid: recording action potentials from the surface of the brain. *Nat. Neurosci.* **18**, 310–315 (2015).
41. Florian, M.C. *et al.* A canonical to non-canonical Wnt signalling switch in haematopoietic stem-cell ageing. *Nature* **503**, 392–396 (2013).
42. Grion, N., Akrami, A., Zuo, Y., Stella, F. & Diamond, M.E. Coherence between rat sensorimotor system and hippocampus is enhanced during tactile discrimination. *PLoS Biol.* **14**, e1002384 (2016).
43. Colgin, L.L. Rhythms of the hippocampal network. *Nat. Rev. Neurosci.* **17**, 239–249 (2016).
44. Henze, D.A. *et al.* Intracellular features predicted by extracellular recordings in the hippocampus *in vivo*. *J. Neurophysiol.* **84**, 390–400 (2000).
45. Bach, M.E. *et al.* Age-related defects in spatial memory are correlated with defects in the late phase of hippocampal long-term potentiation *in vitro* and are attenuated by drugs that enhance the cAMP signaling pathway. *Proc. Natl. Acad. Sci. USA* **96**, 5280–5285 (1999).

ONLINE METHODS

Fabrication of syringe-injectable electronics. The syringe-injectable mesh electronics for chronic brain activity mapping used fabrication procedure and geometrical design similar to our recent reports[32,33]. Key steps involved in the fabrication of syringe-injectable mesh electronics are overviewed in **Supplementary Figure 1**, with the key mesh parameters (**Supplementary Fig. 2**) as follows: total mesh width, W = 2 mm; longitudinal SU-8 ribbon width, w_1 = 20 μm; transverse SU-8 ribbon width, w_2 = 20 μm; angle between longitudinal and transverse SU-8 ribbons, α = 45°; longitudinal spacing (pitch between transverse ribbons), L_1 = 333 μm; transverse spacing (pitch between longitudinal ribbons), L_2 = 125 μm; metal interconnect line width, w_m = 10 μm and total number of recording channels, N = 16. The key fabrication steps (**Supplementary Fig. 1**) are as follows: (i) A sacrificial layer of *Ni* with a thickness of 100 nm was thermally evaporated (Sharon Vacuum, Brockton, Massachussetts) onto a 3″ Si wafer (n-type 0.005 Ω cm, 600-nm thermal oxide, Nova Electronic Materials, Flower Mound, Texas), which was precleaned with oxygen plasma. (ii) Negative photoresist SU-8 (SU-8 2000.5; MicroChem Corp., Newton, Massachussetts) was spin coated on the Si wafer to a thickness of 500 nm, prebaked sequentially at 65 °C for 1 min and 95 °C for 4 min, and then patterned by photolithography (PL) with a mask aligner (ABM mask aligner, San Jose, California). After PL exposure the sample was post-baked sequentially at 65 °C for 3 min and 95 °C for 3 min. (iii) The SU-8 photoresist was then developed (SU-8 Developer, MicroChem Corp., Newton, Massachussetts) for 2 min, rinsed with isopropanol, dried in an N_2 flow and hard baked at 185 °C for 1 h. (iv) The wafer was then cleaned with oxygen plasma (50 W, 1 min), spin coated with MCC Primer 80/20 and LOR 3A lift-off resist (MicroChem Corp., Newton, Massachussetts), baked at 185 °C for 5 min, followed by spin coating Shipley 1805 positive photoresist (Microposit, the Dow Chemical Company, Marlborough, Massachussetts), which was then baked at 115 °C for 5 min. The positive photoresist was patterned by PL and developed (MF-CD-26, Microposit, the Dow Chemical Company, Marlborough, MA) for 90 s. (v) A 1.5-nm thick Cr layer and a 100-nm thick Au layer were sequentially deposited by electron-beam evaporation (Denton Vacuum, Moorestown, New Jersey), followed by a lift-off step (Remover PG, MicroChem Corp., Newton, Massachussetts) to make the Au interconnect lines. (vi) Steps iv and v were repeated for PL patterning and deposition of the Pt-sensing or stimulation electrodes (Cr, 1.5 nm and Pt, 50 nm). The diameter of Pt-sensing electrodes was 20 μm, and that of Pt-stimulation electrodes was increased to 150 μm (the larger diameter was used to afford lower impedance for electrical stimulation). (vii) Steps ii and iii were repeated for PL patterning of the top SU-8 layer, which served as the top encapsulating and insulating layer of the metal interconnect lines. (viii) Subsequently, the Si wafer was cleaned with oxygen plasma (50 W, 1 min) and then transferred to a Ni etchant solution comprising 40% $FeCl_3$:39% HCl:H_2O = 1:1:20 to remove the sacrificial Ni layer and release the mesh electronics from the Si substrate. Released mesh electronics were rinsed with deionized (DI) water, transferred to an aqueous solution of poly-D-lysine (PDL, 1.0 mg/ml, MW 70,000–150,000, Sigma-Aldrich Corp., St. Louis, Missouri) for 24 h and then transferred to 1× phosphate buffered saline (PBS) solution (HyClone Phosphate Buffered Saline, Thermo Fisher Scientific Inc., Pittsburgh, Pennsylvania) before use.

Vertebrate animal subjects. Adult (25–35 g) male C57BL/6J mice (Jackson Laboratory, Bar Harbor, Maine) were the vertebrate animal subjects used in this study. The total number of mice used for demonstrating chronic single neuron level recordings is 4, which was statistically determined by power analysis[46] by assuming a significance level of 5% and an average spike amplitude to variation ratio of 3.0 at 90% power. Moreover, a fifth mouse with two meshes injected was used to show multisite injection stability, a sixth subject was used for stimulation studies, a seventh mouse was used for freely behaving mouse recordings, and three additional mice were used for immunohistochemical studies. Exclusion criteria were pre-established: animals with failed surgery or substantial acute implantation damage (>100 μL of initial liquid injection volume) were discarded from further chronic recordings. Randomization or blinding study was not applicable to this study. All procedures performed on the mice were approved by the Animal Care and Use Committee of Harvard University. The animal care and use programs at Harvard University meet the requirements of the Federal Law (89-544 and 91-579) and NIH regulations and are also accredited by the American Association for Accreditation of Laboratory Animal Care (AAALAC). Animals were group housed on a 12 h:12 h light:dark cycle in the Harvard University's Biology Research Infrastructure (BRI) and fed with food and water *ad libitum* as appropriate.

***In vivo* mouse survival surgery.** *1. Stereotaxic injection of mesh electronics in mouse brain. In vivo* injection of mesh electronics into the brains of live mice was performed using a controlled stereotaxic injection method described previously[33]. First, all metal tools in direct contact with the surgical subject were autoclaved for 1 h before use, and all plastic tools in direct contact with the surgical subjects were sterilized with 70% ethanol and rinsed with sterile DI water and sterile 1× PBS before use. Prior to injection, the mesh electronics were sterilized with 70% ethanol followed by rinsing in sterile DI water and transfer to sterile 1× PBS. The basic procedure for loading the mesh into glass capillary needles is shown schematically in **Supplementary Figure 3**.

C57BL/6J mice were anesthetized by intraperitoneal injection of a mixture of 75 mg/kg of ketamine (Patterson Veterinary Supply Inc., Chicago, Illinois) and 1 mg/kg dexdomitor (Orion Corporation, Espoo, Finland). The degree of anesthesia was verified via the toe pinch method before the surgery started. To maintain the body temperature and prevent hypothermia of the surgical subject, a homeothermic blanket (Harvard Apparatus, Holliston, Massachussetts) was set to 37 °C and placed underneath the anesthetized mouse, which was placed in the stereotaxic frame (Lab Standard Stereotaxic Instrument, Stoelting Co., Wood Dale, Illinois) equipped with two ear bars and one nose clamp that fixed the mouse head in position. Puralube ocular lubricant (Dechra Pharmaceuticals, Northwich, UK) was applied on both eyes of the mouse to moisturize the eye surface throughout the surgery. Hair removal lotion (Nair, Church & Dwight, Ewing, NJ) was used for depilation of the mouse head and iodophor was applied to sterilize the depilated scalp skin. A 1-mm longitudinal incision along the sagittal sinus was made in the scalp with a sterile scalpel, and the scalp skin was resected to expose a 6 mm × 8 mm portion of the skull. METABOND enamel etchant gel (Parkell Inc., Edgewood, New York) was applied over the exposed

cranial bone to prepare the surface for mounting the electronics on the mouse skull later.

A 1 mm diameter burr hole was drilled using a dental drill (Micromotor with On/Off Pedal 110/220, Grobet USA, Carlstadt, NJ) according to the following stereotaxic coordinates: anteroposterior: −4.96 mm, mediolateral: 3.10 mm. After the hole was drilled, the dura was carefully incised and resected using a 27-gauge needle (PrecisionGlide, Becton Dickinson and Company, Franklin Lakes, New Jersey). Then a sterilized 0-80 set screw (18-8 Stainless Steel Cup Point Set Screw; outer diameter: 0.060″ or 1.52 mm, groove diameter: 0.045″ or 1.14 mm, length: 3/16″ or 4.76 mm; McMaster-Carr Supply Company, Elmhurst, Illinois) was screwed into this 1-mm burr hole to a depth of 500 μm as the grounding and reference electrode. Another 1 mm burr hole was drilled for injection of mesh electronics according to the following stereotaxic coordinates depending on specific brain areas for activity recording: (1) Primary somatosensory cortex, barrel field: anteroposterior, −1.82 mm; mediolateral, −3.00 mm; dorsoventral, 0.75 mm. (2) Primary somatosensory cortex, trunk: anteroposterior, −1.70 mm; mediolateral, −2.00 mm; dorsoventral, 0.75 mm. (3) Hippocampal CA1 field: anteroposterior, −1.70 mm; mediolateral, −1.60 mm; dorsoventral, 1.17 mm. (4) Hippocampal CA3 field: anteroposterior, −1.70 mm; mediolateral, −2.00 mm; dorsoventral, 1.85 mm.

The dura was removed from the burr hole drilled for mesh electronics injection, and sterile 1 × PBS was swabbed on the surface of the brain to keep it moist throughout the surgery. The mesh electronics was injected into the desired brain region using a controlled injection method[33]. In brief, the mesh electronics was loaded into a glass capillary needle with inner diameter (I.D.) of 400 μm and outer diameter (O.D.) of 650 μm (Produstrial LLC, Fredon, New Jersey). The glass capillary needle loaded with mesh electronics was mounted onto the stereotaxic stage through a micropipette holder (Q series holder, Harvard Apparatus, Holliston, Massachussetts), which was connected to a 5 mL syringe (Becton Dickinson and Company, Franklin Lakes, New Jersey) through a polyethylene Intramedic catheter tubing (I.D., 1.19 mm and O.D., 1.70 mm). Controlled injection was achieved by balancing the volumetric flow rate (typically 20–50 mL/h), which was controlled by a syringe pump (PHD 2000, Harvard Apparatus, Holliston, Massachusetts), and the needle withdrawal speed (typically 0.2–0.5 mm/s), which was controlled by a motorized linear translation stage (860A motorizer and 460A linear stage, Newport Corporation, Irvine, California). Using the controlled injection method with field of view (FoV) visualization through an eyepiece camera (DCC1240C, Thorlabs Inc., Newton, New Jersey), the mesh electronics was delivered to specific brain regions with elongated morphology along the injection direction with ~20 μm spatial targeting precision. For successful long-term recordings, the total injection volume is usually between 10 and 100 μL. An unexpected large injection volume (>100 μL) could result in brain edema or failure of recovery from acute surgical damage, leading to expulsion of the subject from the study.

2. Electrical connection of syringe-injectable electronics for chronic recordings from awake and restrained mice. After the injection of mesh electronics into the desired region of a mouse brain, the stereotaxic stage was moved to reposition the glass capillary needle over a 16-channel flexible flat cable (FFC, PREMO-FLEX, Molex Incorporated, Lisle, Illinois), and then the remaining mesh electronics was fully expelled from the needle and unfolded onto the FFC to expose the input–output (I–O) connection pads. High-yield bonding of mesh electronics I–O pads to the FFC was carried out using our reported conductive ink printing method[33]. In brief, the print head loaded with carbon nanotube solution (stock no., P093099-11, Tubes@Rice, Houston, Texas) was driven by a motorized micromanipulator (MP-285/M, Sutter Instrument, Novato, California) through a user-written LabVIEW program to print conductive ink automatically and connect each mesh I–O pad to each of the FFC lines to enable independently addressable sensor elements. Failure of mesh I–O unfolding could lead to potential low-yield electrical connection to the FFC interface cable. All printed conductive lines were passivated by METABOND dental cement (Parkell Inc., Edgewood, New York), and then the entire FFC with mesh electronics bonded to the FFC was cemented to the mouse skull with METABOND dental cement. The FFC was folded to reduce its size on the mouse skull. The total mass of the bonded interface cable with mesh electronics is typically 0.2–0.3 g.

3. Electrical connection of syringe-injectable electronics for chronic recordings from freely behaving mice. After the injection of mesh electronics into the desired mouse brain region, the stereotaxic stage was manually moved to reposition the glass capillary needle to a 32-channel Omnetics male connector (A79024-001, Omnetics Connector Corp., Minneapolis, Minnesota) with a weight of ~0.1 g glued on a nonconductive polyethylene terephthalate (PET) flexible substrate with a thickness of ~0.3 mm, and then the remaining mesh electronics was fully expelled from the needle and unfolded onto the flexible substrate with its I–O connection pads facing the horizontal mounting tails of the Omnetics connector. Conductive ink printing was used to bond the mesh electronics I–O pads to 16 horizontal mounting tails of the Omnetics connector as described above for the FFC cable. The 0-80 grounding screw was electrically connected to one of the four preinstalled grounding and reference pins of the Omnetics connector using silver conductive epoxy (MG Chemicals, Burlington, Ontario, Canada). All printed conductive lines were protected by METABOND dental cement before the entire packaged headstage was cemented to the mouse skull with dental cement.

4. Postoperative care. After surgery was complete, antibiotic ointment (WATER-JEL Technologies LLC, Carlstadt, New Jersey) was applied copiously around the wound, and the mouse was returned to the cage equipped with a 37 °C heating pad, and its activity was monitored every hour until it was fully recovered from anesthesia (i.e., until the mouse exhibited sternal recumbency and purposeful movement). Buprenex (Buprenorphine, Patterson Veterinary Supply Inc, Chicago, Illinois) analgesia was given intraperitoneally at a dose of 0.05 mg/kg body weight every 12 h for up to 72 h post brain surgery.

The overall success rate of our surgical procedure is around 70%, with the main causes for failure including (i) an unexpected large injection volume (>100 μL) resulting in brain edema and (ii) failure of mesh I–O unfolding leading to low-yield electrical connection to the FFC interface cable. The surgery success rate will be further improved by (i) better control of injection volume by further reducing the transverse bending stiffness of mesh electronics and (ii) more reliable I–O unfolding and bonding through designs of I–O pads distributions with larger separation.

doi:10.1038/nmeth.3969

Microcomputed tomography. One mouse injected with mesh electronics, where the I–O was bonded to an FFC and then cemented to the mouse skull, was euthanized via intraperitoneal injection of Euthasol at a dose of 270 mg/kg body weight and decapitated. The decapitated mouse head was imaged using an HMXST Micro-CT X-ray scanning system with a standard horizontal imaging axis cabinet (model: HMXST225, Nikon Metrology, Inc., Brighton, Michigan). Imaging parameters were set as 115 kV and 83 μA (with a 0.1-mm copper filter for beam hardening) for scanning the decapitated mouse head. Before scanning, shading correction and flux normalization were applied to adjust the X-ray detector. The CT Pro 3D software (ver. 2.2, Nikon-Metris, UK) was used to calibrate centers of rotation for micro-CT sinograms and to reconstruct all 2D images. VGStudio MAX software (ver. 2.2, Volume Graphics GMbh, Germany) was used for 3D rendering and analysis of the reconstructed images.

***In vivo* chronic brain recording and stimulation in mice.** *1. Chronic brain recording from awake and restrained mice.* Mice with implanted mesh electronics and FFC connector were recorded chronically on a weekly basis, starting from day 7 postinjection and surgery. Mice were restrained in a Tailveiner restrainer (Braintree Scientific LLC., Braintree, Massachusetts) while their head-mounted FFCs were connected to an Intan RHD 2132 amplifier evaluation system (Intan Technologies LLC., Los Angeles, California) through a homemade printed circuit board (PCB). The 0-80 set screw was used as a reference. Electrophysiological recording was made with a 20-kHz sampling rate and a 60-Hz notch filter, while the electrical impedance at 1 kHz of each recording electrode was also measured by the same Intan system.

2. Chronic brain recording of freely behaving mice. Mice with Omnetics connectors were recorded chronically on a weekly basis when they were freely roaming in the cage. For recording, an Intan preamplifier chip (RHD2132 16-Channel Amplifier Board, Intan Technologies LLC., Los Angeles, California) with preinstalled female Omnetics connector was connected directly to the male Omnetics connector cemented on the mouse skull during surgery, and the mouse was allowed to roam in a cage environment not explored previously. Food pellets were placed at random positions inside the cage for each trial. Electrophysiological recordings were made using the same Intan evaluation system with a 20-kHz sampling rate and a 60-Hz notch filter, and they were synchronized with video recording of the mouse's motion inside the cage using a digital camera.

3. Chronic electrical stimulation of mouse brains. Mice injected with mesh electronics incorporating stimulation and recording electrodes were subjected to electrical stimulation and simultaneous electrophysiological recording periodically to week 14 postsurgery. Similar to chronic electrophysiological recording described above, mice were restrained in the Tailveiner restrainer with a head-mounted FFC connected to the Intan RHD 2132 amplifier evaluation system for 12 recording channels, while the other 4 stimulation channels were connected to a homemade stimulator comprising a function generator (Model 33220A, 20 MHz Function/Arbitrary Waveform Generator, Agilent Technologies, Santa Clara, California) that provided stimulus pulse trains with user-defined current, pulse duration and pulse interval. Typical currents used for stimulation ranged from 5–50 μA, followed by an inverted polarity with the same amplitude to provide capacitor-coupled and charge-balanced stimulation[47]. The pulse duration was 1 ms for each phase (positive or negative) with two consecutive pulses spaced by 1 s. Neural responses to stimulus input through one of the four stimulation electrodes were recorded as both local field potentials (LFPs) and single-unit spikes from the 12 recording electrodes from the same injected mesh electronics. The 0-80 set screw was used as a reference for both stimulation and recording.

Data analysis of electrophysiological recording. *1. Data analysis of LFP and single-unit action potential recording.* The electrophysiological recording data was analyzed offline. In brief, raw recording data was filtered using noncausal Butterworth bandpass filters ('filtfilt' function in Matlab) in the 250–6,000 Hz frequency range to extract single-unit spikes[32], in the 0.1–150 Hz range to extract LFP[32], and in the 4–8 Hz range to extract the theta rhythm of LFP[38]. The intrinsic noise distribution of a specific channel was analyzed based on all recording traces bandpass filtered at 250–6,000 Hz, excluding any firing spikes. The correlation coefficient maps of single-unit spike recording traces shown in **Supplementary Figure 5** were calculated based on the standard Pearson product-moment correlation coefficient for time series. Namely, for two spike traces, $Y_1(t)$ and $Y_2(t)$, the correlation coefficient between them is calculated as

$$Corr(Y_1, Y_2) = \frac{\int_{T_1}^{T_2} (Y_1(t) - \bar{Y}_1)(Y_2(t) - \bar{Y}_2)dt}{\sqrt{\int_{T_1}^{T_2} (Y_1(t) - \bar{Y}_1)^2 (Y_2(t) - \bar{Y}_2)^2 dt}} \quad (1)$$

where T_1 and T_2 indicate the starting and ending time of the recording traces, respectively (in **Supplementary Fig. 5**, the time window is 2 s), and

$$\bar{Y}_i = \int_{T_1}^{T_2} Y_i(t)dt / (T_2 - T_1) \quad (i = 1, 2) \quad (2)$$

represents the averaged value of $Y_i(t)$ over the time period between T_1 and T_2.

Single-unit spike sorting was performed by amplitude thresholding of the filtered traces by automatically determining the threshold based on the median of the background noise according to the improved noise estimation method[48]. The average spike amplitude for each recording channel (**Fig. 2b** and **Supplementary Fig. 6e**) was defined as the peak-to-peak amplitude of the spikes for a typical 1-min recording trace. All of the single-neuron spike analyses shown in **Figure 3** and **Supplementary Figures 10** and **12** were carried out based on a 30-min recording session. The peak-to-trough time for each recorded spike was defined as the time interval τ between the major peak (which can be either positive or negative) and the following rebound with opposite polarity (**Fig. 5a**, II, upper left inset). All sorted spikes were clustered to determine the number of single neurons and to assign spikes to each single neuron using the WaveClus software that employs unsupervised superparamagnetic clustering of single-unit spikes[48]. Spikes assigned to the same cluster were coded with the same color and plotted in the first and second principal components (PC1–PC2) plane. The noise distribution of sorted spikes was obtained by plotting the histogram of the difference between each raw spike and average spike waveform at every sampling point.

The deviations of all the identified neuron noise distributions were computed by fitting each noise histogram to a Gaussian distribution.

The L ratio for each cluster of spikes was calculated as follows[49],

$$L_{\text{ratio}} = \frac{L(C)}{N(C)} = \frac{\sum_{i \notin C} 1 - CDF_{\chi 2}(D^2_{i,C})}{NC} \quad (3)$$

where $N(C)$ denotes the total number of spikes in the cluster, $CDF_{\chi 2}$ presents the cumulative distribution function of the χ^2 distribution in an eight-dimensional feature space, and $D^2_{i,C}$ is the Mahalanobis distance of a spike i from the center of the cluster C. The summation goes over the entire set of spikes that do not belong to the cluster. An L ratio of <0.05 is generally considered good cluster separation and isolation[36,49].

The autocorrelation and cross-correlation of raw and average spike waveforms shown in **Supplementary Figures 6**, **8** and **14** were computed based on the standard Pearson product-moment correlation coefficient defined in equation (1) for the 3 ms time series of each spike[23]. A value of 1 indicates identical spike shapes, irrespective of absolute spike amplitudes.

The spiking times of all clustered single-unit action potentials assigned to each cluster (i.e., each single neuron) were used to compute the interspike interval (ISI) histogram under different bin sizes for verification of unit isolation (**Supplementary Fig. 9**, bin size = 1 ms) and extraction of firing rate by fitting the ISI histogram to a first order exponential decay (**Fig. 3c**, bin size = 20 ms)[37]. The instantaneous phase of the theta rhythm of LFP at the location of each single-unit spike that had been assigned to a certain cluster was determined by performing Hilbert transform of the filtered traces in the 4–8 Hz frequency range, and phase locking behavior of single-unit spikes was investigated by plotting their phase distribution in a polar plot[40]. All the extracted phases of individual spikes with respect to theta rhythm LFP in each recording session were subjected to a Rayleigh Z-test, and Ln(Z) values obtained from multiple recording sessions (across different weeks) for each identified neuron were used to test the statistical significance of each neuron's phase-locking behavior[39,50]. A subsequent Rayleigh Z test was then applied to the extracted locked phases from each week's phase distribution from 3 to 34 weeks postinjection to test the chronic stability of each neuron's phase-locking behavior.

2. Data analysis of freely behaving recording. For freely behaving mice, the raw recording data was taken synchronously with mouse video recording and then bandpass filtered before single-unit spikes were sorted and clustered as described above. The video of mouse movement was analyzed with Gaussian blur filter and object tracking algorithm using Matlab to extract the mouse's trajectory and the distance between its head and the food pellet in real time. The firing rate of the electrophysiological recording was then correlated with the mouse's motion trajectory to derive the interaction-dependent firing behavior when the mouse whisked food pellets in its environment. Phase-locking analyses were performed using the same algorithm described above between the single-unit spikes from Channel D (located in the barrel field of somatosensory cortex) and the theta rhythm of LFP from Channel A (located in the hippocampus) shown in **Figure 6** for data recorded when the mouse was whisking food pellets and foraging. These phase-locking results are presented separately for durations of active whisking and nontactile foraging based on dynamic image processing of the video recording the mouse movement in the cage.

3. Data analysis of electrical-stimulus-provoked recording. For analysis of recording data with electrical stimulation, the onset time of each stimulus was determined by the large artifact peak caused by stimulation input picked by all recording electrodes. All stimulation trials were aligned to that peak as $t = 0$ s (where t is the peristimulus time; $t < 0$ denotes before stimulation, and $t > 0$ denotes after stimulation), based on which peristimulus raster plot and poststimulus first spike latency histogram were plotted using Matlab.

Chronic immunohistochemistry. *1. Histology sample preparation.* Mice with implanted mesh electronics at postinjection times of 2, 6 and 12 weeks were anesthetized with ketamine and dexdomitor and were then transcardially perfused with 40 mL 1× PBS and 40 mL 4% formaldehyde (Sigma-Aldrich Corp., St. Louis, Missouri), followed by decapitation. The scalp skin was removed, and the exposed skull was ground for 10–20 min at 10,000 r.p.m. using a high-speed rotary tool (Dremel, Mount Prospect, Illinois). The brain was resected from the cranium and placed in 4% formaldehyde for 24 h and then transferred to 1× PBS for another 24 h at 4 °C to remove remaining formaldehyde. The brain was transferred to incrementally increasing sucrose solutions (10–30%) (Sigma-Aldrich Corp., St. Louis, Missouri) at 4 °C to cryoprotect the tissue, transferred to cryo-OCT compound (Tissue-Tek O.C.T. Compound, VWR, Radnor, Pennsylvania) and then frozen at −80 °C. The frozen sample was then sectioned into 10-μm-thick horizontal slices using Leica CM1950 cryosectioning instrument (Leica Microsystems, Buffalo Grove, Illinois).

2. Immunohistochemical staining and microscopyic imaging. The brain tissue sections were rinsed three times in 1× PBS and blocked in a solution consisting of 0.3% Triton X-100 (Life technologies, Carlsbad, California) and 5% goat serum (Life Technologies, Carlsbad, California) in 1× PBS for 1 h at room temperature. Slices were then incubated with the primary antibodies, rabbit anti-NeuN (1:200 dilution, Abcam, Cambridge, UK), mouse anti-Neurofilament (1:400 dilution, Abcam, Cambridge, UK), rat anti-GFAP (1:500 dilution, Thermo Fisher Scientific Inc., Cambridge, Massachusetts) or rabbit anti-Iba1 (1:250 dilution, Abcam, Cambridge, UK) containing 0.3% Triton X-100 and 3% goat serum overnight at 4 °C. NeuN is a neuron-specific nuclear protein, and it stains the neural somata. Neurofilament is intermediate filament found in neurons, and it stains neural axons. GFAP is glial fibrillary acidic protein, and it stains astrocytes. Iba-1 is a 17-kDa EF hand protein that is specifically expressed in macrophages and microglia, and it is upregulated by the activation of these cells. After incubation, slices were rinsed nine times for a total of 40 min with 1× PBS before they were incubated with the secondary antibodies, Alexa Fluor 488 goat anti-rabbit (1:200 dilution, Abcam, Cambridge, UK), Alexa Fluor 568 goat anti-mouse (1:200 dilution, Abcam, Cambridge, UK) or Alexa Fluor 647 goat anti-rat (1:200 dilution, Abcam, Cambridge, UK) for 1 h at room temperature; the specific choices of secondary antibodies were made based on primary antibodies used to stain a given slice. Slices were rinsed nine times for a total of 30 min after incubation with secondary antibodies before they were mounted on glass slides with coverslips using ProLong Gold Antifade

doi:10.1038/nmeth.3969

Mountant (Life Technologies, Carlsbad, California). The slides remained in the dark at room temperature for at least 24 h before microscopic imaging.

Confocal fluorescence imaging of the samples was acquired on a Zeiss LSM 880 confocal microscope (Carl Zeiss Microscopy GmbH, Jena, Germany). Confocal images were acquired using 488 nm, 561 nm and 633 nm lasers as the excitation sources for Alexa Fluor 488, Alexa Fluor 568 and Alexa Fluor 647, respectively. ImageJ software was used for image analysis. The mesh electronics in each slice was imaged with differential interference contrast (DIC) on the same microscope and is shown with false blue color in the composite images of **Figure 2d** and **Supplementary Figures 7** and **12h**. Fluorescence intensities of Neurofilament, NeuN and GFAP were based on the analysis of zoomed-out images of those shown in **Figure 2d** and **Supplementary Figures 7a** and **12h** with a field of view of 1.2 mm × 1.2 mm. iba-1 results were based on analysis of brain slices shown in **Supplementary Figure 7b** and an adjacent brain slice of the one shown in **Supplementary Figure 12h** with the same field of view. The fluorescence intensities were normalized (value = 1.0, gray dashed horizontal lines in **Fig. 2e** and **Supplementary Fig. 12i**) against the background values 500 μm away from the probe interface for each sample.

46. Cohen, J. *Statistical Power Analysis for the Behavioral Sciences* 2nd edn (Routledge, 1988).
47. Cogan, S.F. Neural stimulation and recording electrodes. *Annu. Rev. Biomed. Eng.* **10**, 275–309 (2008).
48. Quiroga, R.Q., Nadasdy, Z. & Ben-Shaul, Y. Unsupervised spike detection and sorting with wavelets and superparamagnetic clustering. *Neural Comput.* **16**, 1661–1687 (2004).
49. Schmitzer-Torbert, N., Jackson, J., Henze, D., Harris, K. & Redish, A.D. Quantitative measures of cluster quality for use in extracellular recordings. *Neuroscience* **131**, 1–11 (2005).
50. Courtin, J. *et al.* Prefrontal parvalbumin interneurons shape neuronal activity to drive fear expression. *Nature* **505**, 92–96 (2014).